Invited Paper

Nonvolatile holographic storage methods

Ernest Chuang and Demetri Psaltis
California Institute of Technology
Mail-stop 136-93, Pasadena, CA 91125

ABSTRACT

We demonstrate the storage of 1000 holograms in $LiNbO_3$:Fe, recorded at 488nm and read at 633nm to reduce decay during read-out. We minimize Bragg mismatch problems of the two-wavelength scheme by using thin crystals, while combining peristrophic and angle multiplexing to counter the poorer angular selectivity of thin crystals. We find the reduction in read-out decay to be significant, but limited by dark conductivity.

Keywords: Holographic storage, photorefractive materials, two-lambda method, nondestructive read-out.

1 INTRODUCTION

When a photorefractive crystal is used as the recording material in a holographic memory, the recorded gratings decay when illuminated by the read-out beam. Several methods have been developed to address this problem.[1–10] In this paper we use the two-lambda method[8–10] to experimentally demonstrate the long term storage of 1000 holograms. The motivation for using different wavelengths of light for recording and read-out is simple: If a crystal has an absorption spectrum with a substantial variation as a function of wavelength, then we record at a wavelength λ_1 at which the crystal is highly sensitive and read out at a second wavelength λ_2 at which the crystal is relatively insensitive. In this way we reduce the decay of the gratings caused by the read-out illumination.

Implementing the two-lambda method is straightforward for a single grating. Figure 1 shows the two-lambda

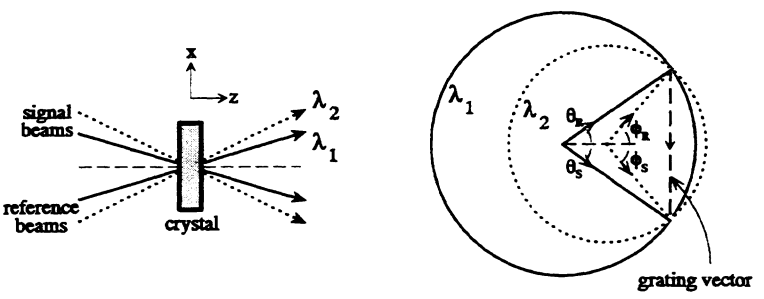

Figure 1: Two-lambda transmission geometry with corresponding k-space diagram. (The diagram assumes that $\lambda_2 > \lambda_1$.)

0-8194-2237-1/96/$6.00

configuration for the transmission geometry, along with the corresponding k-space diagram. Similar diagrams can be readily drawn for the reflection and 90-degree geometries also. A grating is recorded in the usual manner, with signal and reference beams at the first wavelength λ_1. We reconstruct this grating at the second wavelength λ_2, by introducing the read-out beam at a tilted angle with respect to the recording reference beam. We assume that the wavevectors of all the beams lie in the horizontal (x-z) plane. Bragg-matched read-out occurs when the read-out beam is positioned such that the grating vector lies at the intersection of the two k-spheres. The necessary beam angles to achieve Bragg-matched read-out must satisfy the following relationship[10]:

$$\frac{sin[\frac{1}{2}(\theta_s + \theta_r)]}{\lambda_1} = \frac{sin[\frac{1}{2}(\phi_s + \phi_r)]}{\lambda_2} \tag{1}$$

In the above, θ_s and θ_r are the signal and reference beam angles, respectively, at λ_1, and ϕ_s and ϕ_r are the diffracted signal and reference beam angles at λ_2. All angles and wavelengths are defined inside the crystal, with angles measured with respect to the z-axis (the normal to the crystal face).

While we can easily Bragg-match a single grating, when a hologram of an image consisting of many plane wave components is recorded, it is generally impossible to match the entire spectrum simultaneously using a single plane wave read-out reference. In this paper, we show that by using a sufficiently thin crystal and the peristrophic multiplexing[11] technique, a large number of holograms can be stored and recalled with a single plane wave reference.

2 Two-lambda read-out of a complex signal

Recording an image consisting of many plane-wave components can be represented in k-space by a cone of signal vectors that interferes with the reference beam to record a cone of grating vectors, as shown in Figure 2. When we attempt to reconstruct the signal with a reference at λ_2, only the gratings that lie on the circle of intersection between the two k-spheres is exactly Bragg-matched. Hence, only an arc of the signal cone will be reconstructed.

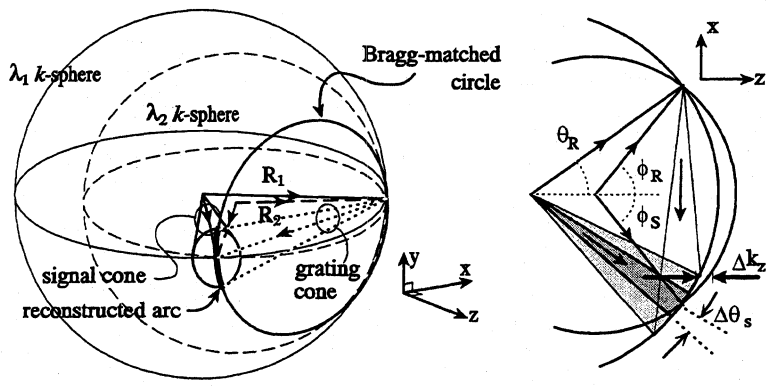

Figure 2: k-sphere diagram for the Bragg-matched condition using two wavelengths

The diffracted intensity, I_{diff}, of the hologram reconstruction at λ_2 is given by

$$I_{diff} \sim sinc^2[\frac{L}{2\pi}\Delta k_z] \tag{2}$$

where L is the crystal thickness and Δk_z is the parameter that determines the degree of Bragg-mismatch. For a plane-wave component in the signal beam whose k-vector lies in the x-z plane and is offset from the central DC

component by $\Delta\theta_s$, the Bragg-mismatch, Δk_z, is given by,

$$\Delta k_z = 2\pi \left\{ \frac{cos\phi_r}{\lambda_2} + \frac{cos(\theta_s + \Delta\theta_s) - cos(\theta_r)}{\lambda_1} - \sqrt{\left(\frac{1}{\lambda_2}\right)^2 - \left[\frac{sin\phi_r}{\lambda_2} - \frac{sin\theta_r + sin(\theta_s + \Delta\theta_s)}{\lambda_1}\right]^2} \right\} \quad (3)$$

For $\Delta\theta_s = 0$, $\Delta k_z = 0$ if equation (1) is satisfied and I_{diff} is maximum. As $\Delta\theta_s$ increases, the diffracted power decreases. Equating Δk_z to $2\pi/L$ and solving for $\Delta\theta_s$ yields the angular location of the first null of equation (2) within the signal cone. If we make the approximation that $\lambda_1, \lambda_2 \ll L$ (which is almost always true for the wavelengths and crystals that we use in practice), then the angular bandwidth of the main lobe of the sinc function can be approximated by

$$sin\Delta\theta_{so} = \frac{\lambda_1 cos\phi_s}{Lsin(\phi_r - \theta_r)} \quad (4)$$

Essentially, $\Delta\theta_{so}$ is the usable bandwidth of the signal cone in the x-z plane. Note that once we select λ_1 and λ_2 we can still make the signal bandwidth arbitrarily high by decreasing L. Therefore there is a trade-off between the usable signal bandwidth and the number of holograms that can be angularly multiplexed at one location. Also note that ϕ_s and ϕ_r are not independent variables – they are determined by the recording beam angles, θ_s and θ_r, and wavelengths, λ_1 and λ_2.

The effect on the reconstructed image of limiting the bandwidth of the signal cone depends on whether we record in the Fourier plane or image plane. We first consider the case of recording in the Fourier plane (Figure 3a). When we record in the Fourier plane, each plane wave component of the signal beam entering the crystal corresponds to a spatial location (pixel) on the input image. Hence, if we reconstruct only a limited angular bandwidth $\Delta\theta_{so}$ of the signal cone in the x-dimension (neglecting variation in the y-direction), we expect to reconstruct a strip of the image, limited in the x-dimension. An example of such a reconstruction is shown in Figure 3b. From the figure we see a slight curvature to the reconstruction in the y-dimension as well as side lobes from the *sinc* modulation in the x-dimension. The curvature that is experimentally observed is due to the fact that the intersection of the two k-spheres in Figure 2 is a circle and a small arc of this circle is spanned by the signal cone. This effect was neglected in the above derivation (Eqs. (1)-(4)).

From the system geometry, we can derive the width of the input image strip that is reconstructed,

$$W = \frac{2Fn\, sin\Delta\theta_{so}}{\sqrt{1 - n^2 sin^2\Delta\theta_{so}}} \quad (5)$$

where F is the focal length of the Fourier transforming lens and n is the refractive index of the material. We assume the crystal to be in air and the central component of the signal beam to be on axis. For signals tilted from the crystal normal, equation (5) must be adjusted for variations due to Snell's law. In Figure 3c we show how the entire image can be sequentially scanned by changing the angle of the read-out reference to reveal different portions or strips of the stored image.

Recording in the image plane (Figure 4a) is analagous to recording in the Fourier plane, except that in place of the input image we would have its Fourier transform. Therefore, instead of reconstructing a strip of the image, we reconstruct a "strip" or band of the frequency spectrum of the image. If we position the read-out reference to Bragg-match the DC component of the image, the resulting reconstruction will be a low-pass filtered version of the original in the x-dimension. Figure 4b compares the reconstruction by the second wavelength to that when read by the original (recording) reference. Note the blurring of the edges in the x-dimension that results from the loss of the high-frequency components of the input signal. From the diffraction relation for a pixel of width δ_x,

$$sin\,\alpha = \frac{\lambda}{\delta_x} \quad (6)$$

where α is the diffraction angle, we equate α to $\Delta\theta_{so}$ in equation (4) and solve for δ_x to obtain the minimum pixel width that can be reconstructed by the second wavelength,

$$\delta_{x,min} = \frac{Lsin(\phi_r - \theta_r)}{cos\phi_s} \quad (7)$$

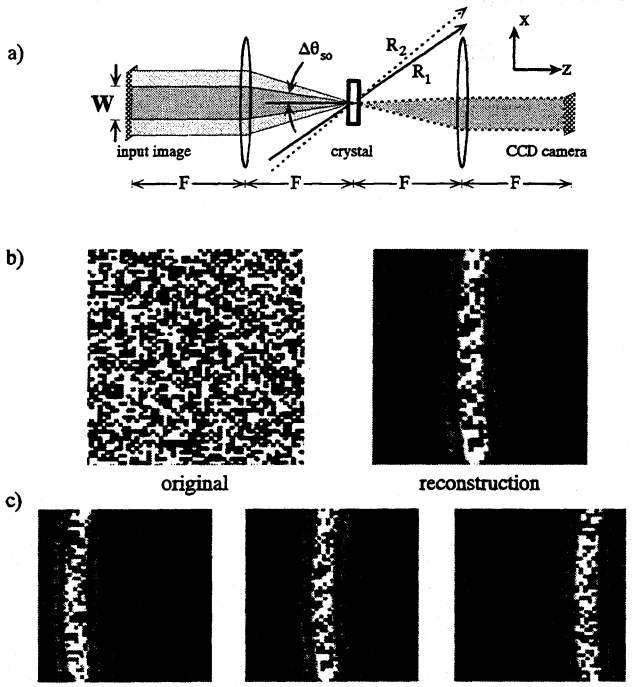

Figure 3: Recording in the Fourier plane: a) diagram of a basic Fourier-plane setup, b) original input image and reconstruction by second wavelength, c) reconstruction of different strips by detuning the angle of the reference beam.

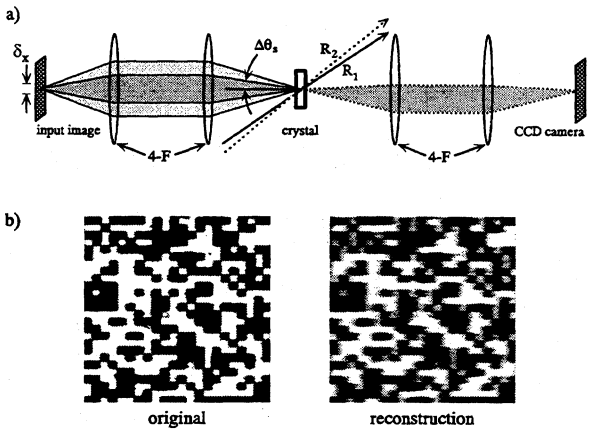

Figure 4: Recording in the image plane: a) diagram of a basic image-plane setup, b) reconstructions by the original recording wavelength (488nm) and second read-out wavelength (633nm).

Similar to the Fourier case, we can also scan the reference beam to bandpass different frequency components of the original image.

A number of solutions have been proposed for the Bragg-mismatch problem of the two-wavelength scheme. Most have dealt with Fourier-plane recording, such as using spherical read-out beams[8] to Bragg-match a larger range of the signal cone or interleaving strips from adjacent holograms.[10] However, we can recover all of the necessary information by recording in the image plane, without the added complexity of the above methods, if we simply adjust the system parameters according to the resolution of the images that we wish to store.

From equation (4) we see that we can maximize $\Delta\theta_{so}$ by:

1. reducing crystal thickness, L,
2. using wavelengths λ_1 and λ_2 that are close together, or
3. reducing the angle between the signal and reference beams.

The second and third options may not always be viable solutions because of the crystal absorption spectrum requirements and angular multiplexing needs. However, we can change the crystal thickness.

Figure 5a shows a reconstruction of a random bit pattern with four regions of different pixel sizes, from 50μm to 200μm square, recorded in a crystal of thickness L=4.6μm. The recording parameters were λ_1'=488nm, λ_2'=633nm (wavelengths in air), $\theta_s = 0°$, and $\theta_r = 11.6°$, which correspond to a theoretical minimum acceptable

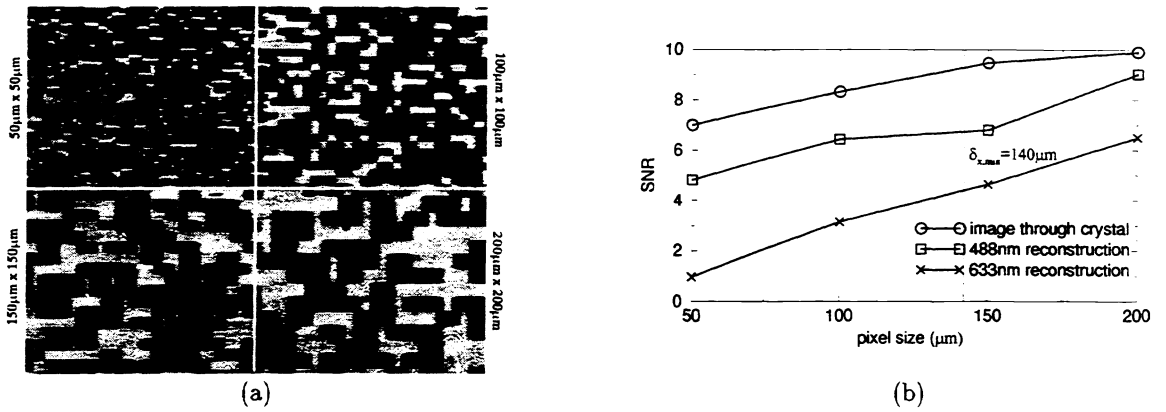

Figure 5: Reconstruction (a) of an image with varying pixel sizes, and (b) plot of SNR vs. pixel size.

pixel size of $\delta_{x,min} \approx 140\mu$m. From the figure we see that while the edge-blurring always exists in the x-direction, we can still easily distinguish between on and off pixels for the 150μm and 200μm pixels, but we get a progressive loss of detail for smaller pixel sizes. Figure 5b shows how the SNR of the images vary with pixel size. Depending on the SNR requirements of the application for which this storage method is being used, we can choose the pixel size that we use in order to achieve this SNR. If an application required a higher resolution than a given crystal could accommodate, then we could simply switch to a thinner crystal, according to equation (7).

Figure 6 shows two image-plane reconstructions of the same image – one recorded in a 4.6mm-thick crystal and another in a 0.25mm-thick crystal. Using the same recording geometry as was used for Figure 5, $\delta_{x,min}$ for the thinner crystal is 7.6μm compared to 140μm for the thicker crystal. This is evident in the figure, where the reconstruction with the thinner crystal preserves the higher spatial frequencies, so that the edge-blurring is hardly noticeable. Rectangular pixels were used for these images to demonstrate that the pixel-size limitation is indeed only in the x-dimension; even the thicker crystal reconstructs high spatial frequencies cleanly in the y-dimension.

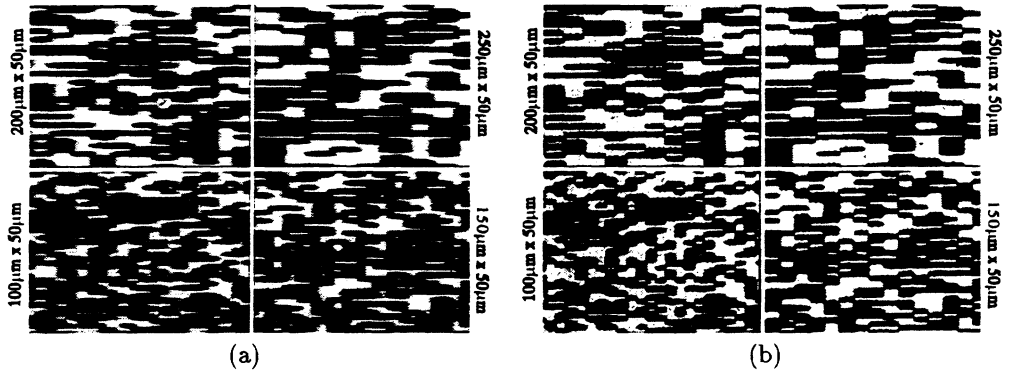

Figure 6: Image-plane reconstructions at 633nm using a 4.6mm thick crystal (a) and a 0.25mm thick crystal (b).

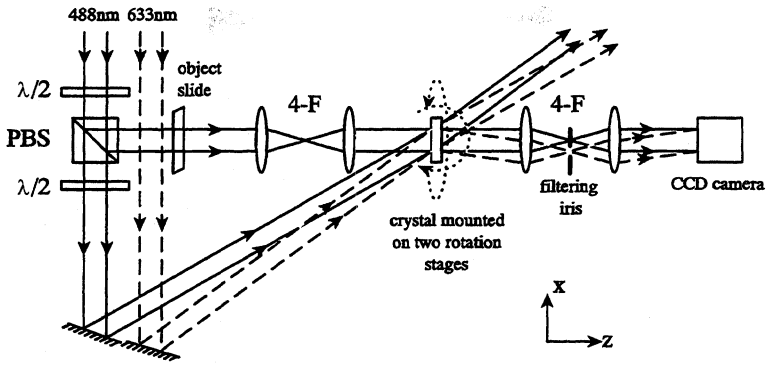

Figure 7: Experimental setup for 1000-hologram experiment using the two-lambda architecture.

3 EXPERIMENT

Figure 7 shows the experimental setup used for the two-lambda image-plane architecture. It consists of two 4-F systems to image the input object through the crystal and onto the CCD detector, with two offset beam paths for the recording and read-out reference arms. We used λ_1'=488nm polarized out-of-plane for recording and λ_2'=633nm polarized in-plane for read-out, provided by an argon ion and He-Ne laser, respectively. The photorefractive crystal was a $LiNbO_3 : Fe$ (0.015%) crystal, 4.6mm thick, cut from a boule from CrystalTech. The crystal was mounted on two rotation stages – one to provide angular tilt and the other for peristrophic tilt. We combined peristrophic multiplexing with angle multiplexing to compensate for the loss in angular selectivity from using thinner crystals. The angle between the recording signal and reference beams outside the crystal was 28.3°, with the signal on axis and the crystal c-axis in the x-z plane defined to be the "origin" around which the angular and peristrophic rotations were referenced.

The measured angular selectivity for this geometry was $\Delta\phi = 0.035°$ for the first null with the 633nm reference. However, in the experiment we used angular offsets of 0.2° to space the holograms past the 5th null in order to minimize cross-talk. The theoretical peristrophic selectivity was $\Delta\psi = 0.79°$, whereas in practice we used peristrophic spacings of 2° to avoid cross-talk from the sidelobes of the Fourier transform. Using 50 angular locations (from −4.9° to +4.9° tilt) and 20 peristrophic locations (from −9° to +9° and 171° to 189°), we recorded 1000 holograms using a 150μm-pixel random bit pattern mask as input.

Figure 8 shows the resulting comb function recorded using an exposure schedule. The diffraction efficiencies are fairly uniform at about 6×10^{-6}. Of the 1000 holograms, we visually inspected about 100 for uniformity and randomly chose five for SNR and probability-of-error analysis. Figure 9 shows the original input image as seen through the crystal, a sample reconstruction at 488nm, and two reconstructions at 633nm. For hologram #263, we also show histograms for the 488nm and 633nm reconstructions below their respective images.

SNR was measured by averaging CCD pixel values within each image pixel and then dividing the mean by the variance of the averaged pixel values. Probability of error was calculated assuming Gaussian distributions to the histograms. For the reconstructions that were read out with the original reference at 488nm, the SNR ranged from approximately 3.0 to 4.0, with corresponding probabilities of error from 10^{-3} to 10^{-4}. The results for the reconstructions at 633nm were better than those at 488nm, despite the low-pass filtering effect of the two-lambda image-plane readout. For the 633nm reconstructions, the SNR varied from 3.5 to 5.5, with probabilities of error from 10^{-5} to 10^{-7}.

There are a few reasons for the apparent improvement in reconstruction quality using 633nm as opposed to 488nm. One reason is the method used for averaging pixel values in the reconstructions; the program that we

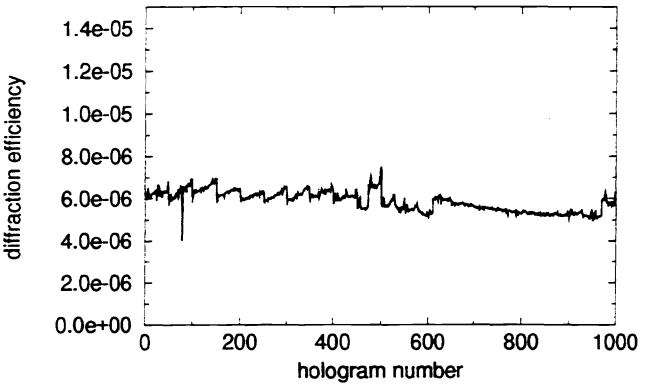

Figure 8: Experimental comb function for 1000 holograms.

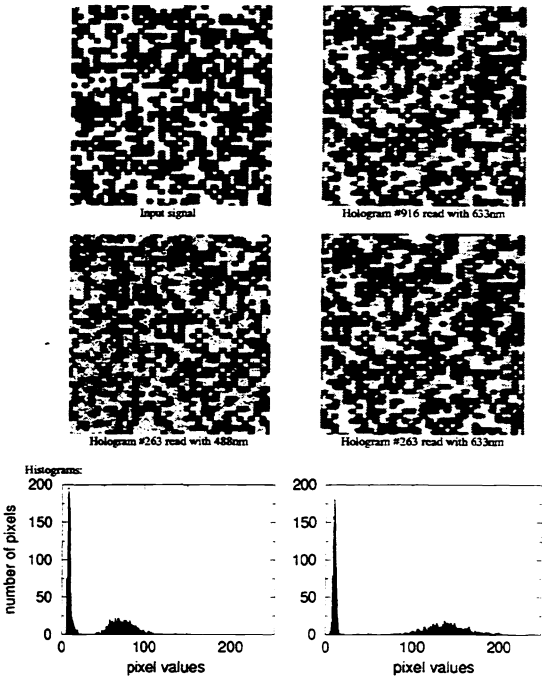

Figure 9: Sample reconstructions and histograms from the 1000-hologram experiments.

used to calculate SNR averages CCD pixels only within a margin of each image pixel – edge values are discarded. Hence, any blurring effect at the edges of pixels in the x-dimension becomes less of a factor for the SNR and error calculations. Another reason is that the 488nm reference was out-of-plane (ordinary) polarized, whereas the 633nm reference was in-plane (extraordinary) polarized, resulting in a higher diffraction efficiency for the 633nm readout. Yet another factor is that the crystal has a larger effective scattering cross-section for blue light than for red.

4 ERASURE

We now examine how well this two-lambda architecture reduced the decay rate due to the read-out illumination. We recorded two holograms with the same exposure at 488nm, and erased one with a non-Bragg-matched beam at 488nm and the other with an equal intensity (21.4mW/cm^2) beam at 633nm, periodically monitoring the grating strength by scanning for the reconstruction peak with a 633nm read-out beam. The decay rate was also measured with no erasure beam in order to determine the decay contribution from dark conductivity as well as from the monitoring beam. The decay characteristics are plotted in Figure 10b. The measured erasure time constant (which includes the effects of dark erasure) for the 488nm erasure was $\tau'_{e,488} = 3.21$hrs, while that for the 633nm erasure was $\tau'_{e,633} = 35.6$hrs, giving a reduction in the read-out decay rate by a factor of 11.1. However, after factoring out the dark decay ($\tau_{e,dark} = 194$hrs), modelling the erasure as,

$$e^{-t/\tau'_e} = e^{-t/\tau_e} e^{-t/\tau_{e,dark}} \tag{8}$$

where τ'_e is the measured erasure time constant including dark effects, τ_e is the erasure time constant due to the erasing illumination, and $\tau_{e,dark}$ is the erasure time constant due to the dark conductivity and erasure from the monitoring beam, we find the actual contribution caused by the illumination to be $\tau_{e,488} = 3.27$hrs and $\tau_{e,633} = 43.6$hrs, corresponding to a ratio of 13.3.

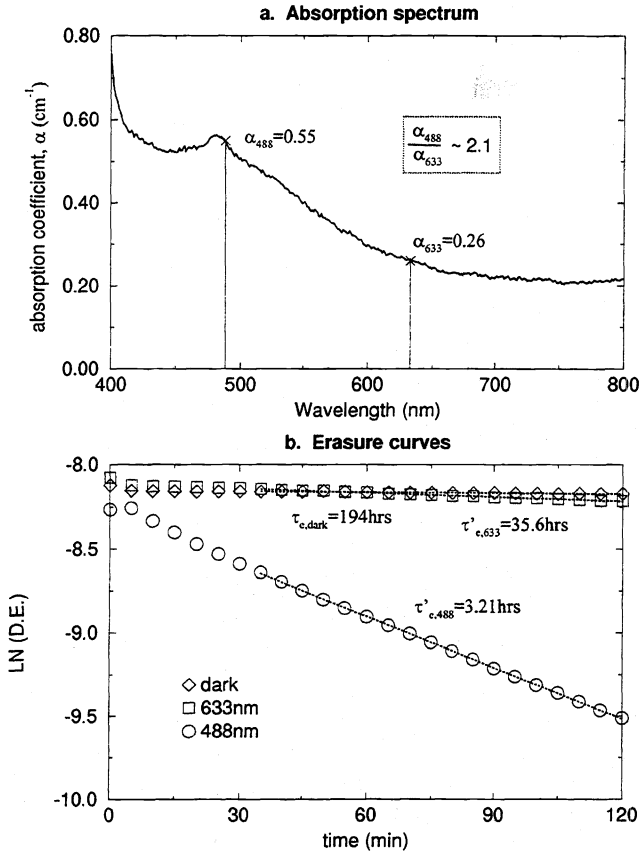

Figure 10: a) Absorption spectrum and b) erasure curves for $LiNbO_3$:Fe sample.

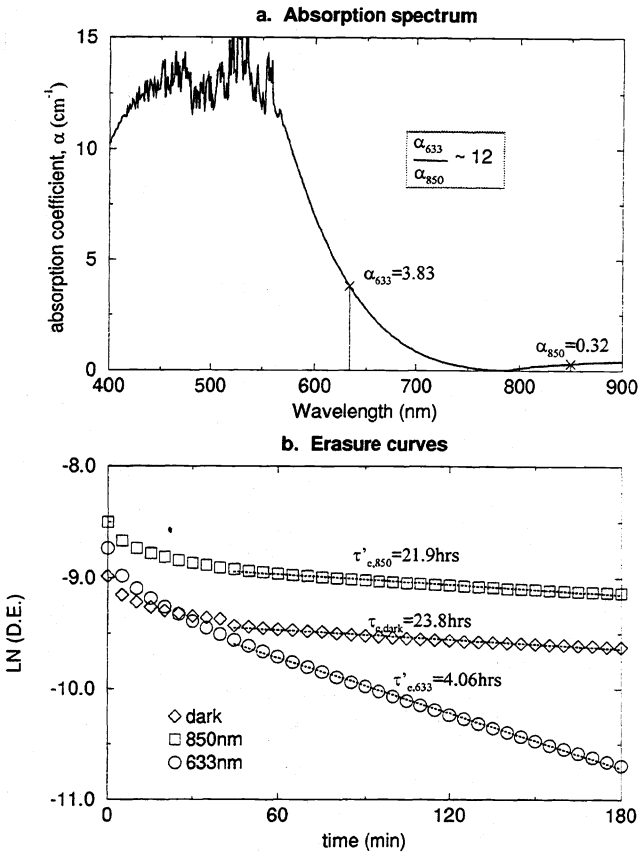

Figure 11: a) Absorption spectrum and b) erasure curves for $LiNbO_3$:Fe:Ce sample.

The absorption spectrum for this crystal is shown in Figure 10a. For the two wavelengths used in our experiment, the absorption coefficients were $\alpha_{488} = 0.55\text{cm}^{-1}$ and $\alpha_{633} = 0.26\text{cm}^{-1}$. The ratio of these coefficients is 2.1, so the ratio of 13.3 in erasure time constants was larger than expected. At this point we haven't developed a theoretical model to predict relative erasure times from the absorption spectrum. However, it should not be entirely surprising that the ratio of absorption coefficients is different from that of the erasure time constants, since not every photon that is absorbed will contribute toward the erasure of the hologram. For example, some energy will be absorbed by the lattice, or an electron may be excited into the conduction band but immediately be trapped again. Still, we expect that larger ratios in absorption coefficients will be reflected in larger ratios in erasure time constants.

One important note is that the choice of crystal and wavelengths used in this experiment was not optimized for the two-lambda architecture, but was based simply on what was available in the lab. The crystal was one that we have had good results with in the past, and 488nm and 633nm were laser wavelengths that were readily at hand with good power output. However, to maximize the benefits of the two-lambda scheme, we can certainly be more selective in our choice of crystal and system parameters.

For instance, Figure 11a shows the absorption spectrum for a doubly-doped $LiNbO_3$:Fe:Ce (0.05% Fe, 0.03% Ce) crystal from Deltronic that we have begun to use in experiments. This crystal exhibits a much wider range of absorption coefficients over the same range of wavelengths than the crystal that we used for the 1000 hologram experiment. We tested this crystal using $\lambda_1' = 633\text{nm}$ for recording and $\lambda_2' = 850\text{nm}$ for read-out, corresponding to absorption coefficients of $\alpha_{633} = 3.83\text{cm}^{-1}$ and $\alpha_{850} = 0.32\text{cm}^{-1}$, respectively. This gives a ratio of 12.0 of absorption coefficients, nearly six times that for the previous crystal and wavelengths.

Figure 11b shows the erasure characteristics that we measured for the two wavelengths, using equal intensities of 15.7mW/cm^2, as well as for the dark erasure. From the data we obtain the erasure time constants (including dark effects), $\tau'_{e,633} = 4.06$hrs and $\tau'_{e,850} = 21.9$hrs. Again, factoring out the dark erasure ($\tau_{e,dark} = 23.8$hrs) according to relation (8) to get the true decay contributions due to the illumination, we get $\tau_{e,633} = 4.79$hrs and $\tau_{e,850} = 273.4$hrs, giving a reduction in the erasure rate by a factor of 57.1.

These results are encouraging because they show that we can indeed greatly reduce the read-out decay by using a second wavelength for read-out at which the crystal is much less absorptive. However, it also illustrates a fundamental limitation of the two-lambda scheme, and that is the problem of dark erasure. While it may be true that the read-out wavelength slows the erasure *due to the read-out illumination* by a factor of nearly 60, unless something can be done to reduce the dark decay we will not observe this improvement in practice. Instead, we will remain limited by the time constants with dark erasure, $\tau'_{e,633}$ and $\tau'_{e,850}$, which only offer a reduction by a factor of 5.5 in erasure time. In this case, the first crystal would be a better option due to its lower dark conductivity.

5 CONCLUSION

A two-lambda architecture can significantly reduce the decay of holograms due to readout. However, such an architecture does introduce new complexities and problems to the system, some of which we addressed here while others still require further investigation. On the system side, we have shown that the Bragg-mismatch problem of the two-lambda scheme can be minimized by properly adjusting system parameters, primarily the thickness of the crystal. We also combine peristrophic with angle multiplexing to counter the poorer angular selectivity of thin crystals. Also, by recording holograms in the image plane, we can retrieve entire data pages at a time with a simple plane-wave readout beam, without the added complexity of using spherical beams or interleaving holograms.

Two main problems remain, however. The first is the problem of dark conductivity. As was shown earlier, dark erasure can severely limit the effectiveness of the second wavelength at reducing the decay rate. Furthermore, the dark erasure prevents a two-lambda architecture from truly maintaining a constant grating strength, since at best it can only eliminate the erasure from the readout process. In contrast, periodic copying[4–7] for instance can restore the strength of holograms regardless of the cause of the holographic decay – whether it is due to readout or dark conductivity. Hence, a two-lambda scheme will probably be most useful when used in conjunction with some other process, such as copying, so as to expand the time frame over which we can refresh the holograms. It may be possible to affect the dark conductivity by changing the crystal temperature, impurity doping level, or oxidation/reduction state.

The second problem is the density limitation. Because of the $\delta_{x,min}$ constraint, the two-lambda system will restrict the storage density of the system except where very thin crystals are being used. Alternatively, if the crystal exhibits sharp changes in absorption behavior for small changes in wavelength, then the density can approach that of a one-wavelength system. Otherwise the two-lambda system will be most useful for storing large numbers of low-density holograms.

6 ACKNOWLEDGEMENTS

We would like to thank Geoffrey Burr and Allen Pu for helpful discussion. Ernest Chuang also acknowledges the support of a National Science Foundation fellowship.

7 REFERENCES

[1] J. J. Amodei and D. L. Staebler. "Holographic pattern fixing in electro-optic crystals". *Applied Physics Letters*, 18(12):540–542, June 1971.

[2] F. Micheron and G. Bismuth. "Electrical control of fixation and erasure of holographic patterns in ferroelectric materials". *Applied Physics Letters*, 20(2):79–81, January 1972.

[3] D. von der Linde, A. M. Glass, and K. F. Rodgers. "Multiphoton photorefractive processes for optical storage in linbo$_3$". *Applied Physics Letters*, 25(3):155–157, August 1974.

[4] D. Brady, K. Hsu, and D. Psaltis. "Periodically refreshed multiply exposed photorefractive holograms". *Optics Letters*, 15(14):817–819, July 1990.

[5] H. Sasaki, Y. Fainman, J.E. Ford, Y. Taketomi, and S. Lee. "Dynamic photorefractive optical memory". *Optics Letters*, 16(23):1874–1876, December 1991.

[6] S. Boj, G. Pauliat, and G. Roosen. "Dynamic holographic memory showing readout, refreshing, and updating capabilities". *Optics Letters*, 17(6):438–440, March 1992.

[7] Y. Qiao and D. Psaltis. "Sampled dynamic holographic memory". *Optics Letters*, 17(19):1376–1378, October 1992.

[8] H. Külich. "Reconstructing volume holograms without image field losses". *Applied Optics*, 30(20):2850–2857, July 1991.

[9] R. McRuer, J. Wilde, L. Hesselink, and J. Goodman. "Two-wavelength photorefractive dynamic optical interconnect". *Optics Letters*, 14(21):1174–1176, November 1989.

[10] D. Psaltis, F. Mok, and H. Li. "Nonvolatile storage in photorefractive crystals". *Optics Letters*, 19(3):210–212, February 1994.

[11] K. Curtis, A. Pu, and D. Psaltis. "Method for holographic storage using peristrophic multiplexing". *Optics Letters*, 19(13):993–994, July 1994.